RESEARCH ARTICLE

Fabrication of 1D graphene nanoribbon and malenized linseed oil-based nanocomposite: a highly impervious bio-based anti-corrosion coating material for mild steel

Ningappa Kumara Swamy[1,2] · Kikkeri Narasimha Shetty Mohana[1] · Mahesh Bhaskar Hegde[1] · Ambale Murthy Madhusudana[1]

Abstract

Graphene nanoribbon (GNR) is a flat ribbon-like 1D nanomaterial of graphene family rarely explored in the development of anti-corrosion coatings. In the present work, a bio-based anti-corrosion coating was fabricated using GNR as nanofiller in malenized linseed oil (MLO) polymer network. MLO polymer network was first prepared from commercially available linseed oil by malenization reaction at 80 °C using maleic anhydride. Later, GNR was synthesized from multiwalled carbon nanotube by oxidative unzipping method and incorporated into MLO polymer network to obtain the bio-based MLO–GNR nanocomposite. The as-prepared MLO and MLO–GNR coating materials were spin coated onto bare mild steel samples and cured at 80 °C for 24 h. The morphology and surface characteristics of coatings were studied by spectroscopic and microscopic techniques. Further, the anti-corrosion behaviour of bare and coated MS samples was investigated by potentio-dynamic polarization and electrochemical impedance methods in a 3.5% NaCl medium. Among the samples, MLO–GNR-coated samples exhibited a high level of corrosion inhibition in the saline medium compared to uncoated MS sample as the damages and destruction activity were more on its surface than their counterparts. MLO–GNR nanocomposite coating exhibited robust corrosion resistance activity and showed 99.9% protection efficiency. Further, the MLO–GNR coating displayed higher stability in the saline medium as well as open-air environment establishing that the flat GNR molecule acts as excellent nanofiller in MLO polymer network to produce robust anti-corrosion activity leading to protection of mild steel.

✉ Kikkeri Narasimha Shetty Mohana
  drknmohana@gmail.com

1 Department of Studies in Chemistry, University of Mysore, Mysuru, Karnataka 570006, India

2 Department of Chemistry, JSS Science and Technology University, Mysuru, Karnataka 570006, India

Graphical abstract
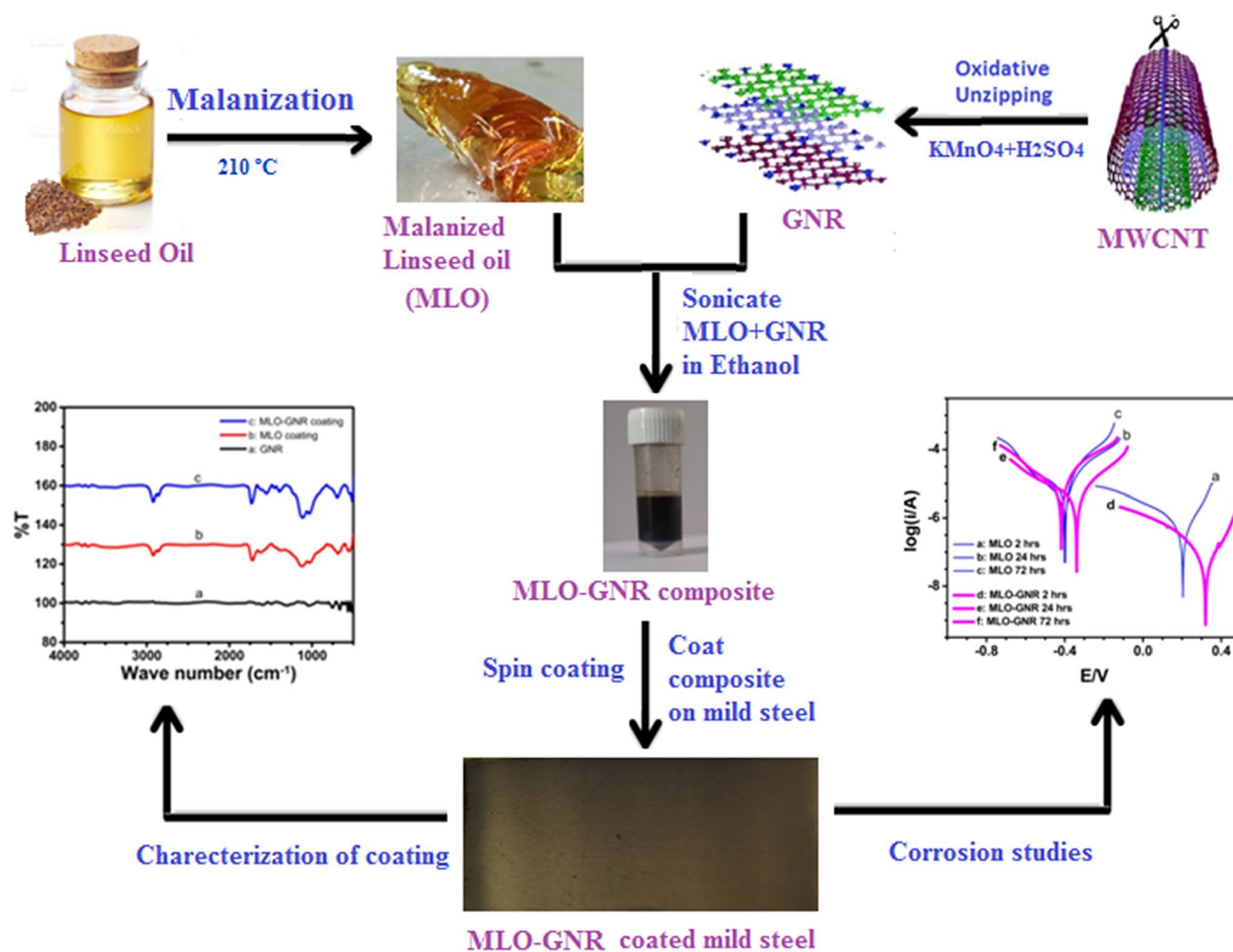
1 Introduction

Protection of steel from corrosion is a long-standing unresolved issue in many domestic and engineering applications namely power production, petroleum, marine, pipeline, aerospace, automobiles, electrochemical industries, construction industries and so forth [1]. Though several coating materials viz nanocomposite coatings, hydrophobic coatings and organic–inorganic hybrids have been explored and proven to enhance the life of steel, there is still exigency for simple, scalable, cost-effective and environment-friendly corrosion protection materials and techniques for industrial application [1–3].

Organic coatings offer protection to metals by acting as an effective physical barrier between the metal surface and the corrosive environment. However, the coating barrier performance often declines due to the diffusive migration of corrosive species such as oxygen, water and chloride ions into the metal-coating interface through coating porosities [4]. There have been attempts to enhance the barrier performance and anti-corrosion properties of these coatings through insertion of various nanofillers, additives and/or anti-corrosive pigments into the coating matrix [4–7]. The nanofiller insertions have been reported to enhance the protective properties of coatings by several means such as increasing the diffusion path length of electrolyte, reducing cavities and micro-pores and/or increasing cross-linking density. By reducing porosity and extending the diffusion path length, the nanofillers reduce the diffusion of ions and water into metal-coating interface, thereby bringing down the coating adhesion loss [7, 8].

Organic coatings derived from natural products, apart from being anti-corrosive, offer some advantages such as low cost, non-toxic, abundance, eco-friendliness, and therefore can be effective alternatives to petro-based polymer coatings. Several authors have reported the use of vegetable oils as renewable raw materials for the synthesis of polymers [9–13]. Vegetable oils can be the competing alternative to the petro-based polymer products due to their diverse abundance and the functional group flexibilities in their backbone structure such as double bonds, epoxies and hydroxyls which pave way for variety of modifications through chemical reactions [13, 14].

Linseed oil (LO) is a triglyceride made up of 51–55% triply unsaturated α-linolenic acid, 18–22% doubly unsaturated oleic acid, 14–17% monounsaturated linoleic acid, 7% saturated palmitic acid and 3–4% stearic acid. LO is an excellent raw material for the preparation of polymers due to the presence of di- and tri-unsaturated esters in larger proportions [15, 16]. For the present work, a green organic coating material was prepared by subjecting LO to malenization reaction and its anti-corrosive behaviour was investigated.

In recent years, researchers have employed several carbon-based nanomaterials viz. graphene oxide, carbon nanotubes, carbon nanofibers, etc., as nanofillers to improve anti-corrosion performance of polymer coatings. The carbon-based nanomaterials have been proved to show good barrier properties due to their large specific surface area [6, 7, 14, 16, 17].

Among the carbon-based nanomaterials, GNR is a newly discovered quasi-one-dimensional graphene-like carbon-based nanomaterial with a ribbon-type structure. Unlike graphene sheets, GNRs possess narrower width, dense and abundant edge defect sites with superior chemical reactivity [18–20].The high surface area of GNRs coupled with a high density of reactive edges and defects on the surface makes it potential nanofiller for anti-corrosive applications. GNR is reported as nanofiller in polyurethane (PU) coating and it is found to enhance the mechanical properties and the anti-corrosive behaviour of PU coating [21]. Some of the GNR-based reinforcements and nanocomposites reported in literature such as GNR/PVDF [22], PEG-GNR [23], GNR@CeO$_2$ nanocomposite [24] and GNR-CoB nanocomposite [25] have respectively shown EMI shielding, wound healing, sono-photocatalytic and sensing properties. However, unlike graphene and other carbon-based nanomaterials, the GNR is very less explored as nanofiller in anti-corrosive coating applications. Keeping this in view, we have synthesized meleinized linseed oil (MLO) polymer network by malenization of linseed oil and investigated its potentials as an anti-corrosion coating material for mild steel in the saline medium. Further, for the first time, we have used GNR as the nanofiller in MLO coating matrix and investigated its effect on anti-corrosion properties in the saline medium.

The results showed that the MLO coating exhibit good anti-corrosive characteristics and the incorporation of GNRs enhanced the performance characteristics of the coating.

2 Experimental section

2.1 Materials and instruments

Multi-walled carbon nanotube (MWCNT), potassium permanganate (KMnO$_4$) and maleic anhydride were procured from Sigma-Aldrich. The analytical grade reagents conc. sulphuric acid (H$_2$SO$_4$) and hydrogen peroxide (H$_2$O$_2$) used in study were purchased from Fischer Scientific. LO was purchased from Deve Herbes, New Delhi, India. The mild steel panels (1 mm thickness) with an elemental composition of Fe (99.6%), Mn (0.12%), Al (0.1%), S (0.012%), C(0.05%), Si (0.05%) and P (0.010%) were used in the study.

The ^{1}H-NMR spectral characterization of LO and MLO was performed with Agilent 400MR DD2 instrument. The powder X-ray diffraction (XRD) studies were conducted using 3-kW Rigaku D/max2200PC diffractometer (λ = 1.54 Å, Cu–Kα radiation). Fourier-transform Infrared spectroscopy (FTIR) analysis was performed in the wave number range of 4000–400 cm^{-1} using Perkin Elmer FTIR spectrometer. Raman spectra of samples were recorded using Lab Spec-6 instrument. Morphological features of GNRs and coatings were studied by High-resolution Transmission electron microscopy (HR-TEM, Instrument: JEOL/JEM2100), Scanning electron microscopy (SEM, Instrument: ZEISS EVO LS-15) and Atomic force microscopy (AFM, Instrument: Hitachi S-3400N). Thermal analysis of the coatings was performed using Q-500 TA Instruments (USA). All electrochemical investigations were carried out using CH1608E electrochemical work station (Austin, USA).

2.2 Synthesis of GNRs by unzipping MWCNTs

GNRs were synthesized from MWCNTs via a two-step unzipping process described in the literature [26]. 300 mg of MWCNTs were mixed with 120 ml conc. H$_2$SO$_4$ (98%) under constant stirring condition at room temperature for about 24 h to get a slurry-like material. Later, 1.5 gm of KMnO$_4$ was slowly introduced to slurry and heated to 85 °C for 4 h under vigorous stirring conditions. The resulting hot slurry was diluted to 400 ml with deionized water and then kept in an ice bath for 30 min under constant stirring. The mixture was removed from ice bath and 60 ml of H$_2$O$_2$ was added to it followed by dilution with 200 ml deionized water. Further, the reaction mixture was cooled and washed, and centrifuged with 10% HCl. The centrifuged sample was washed repeatedly using deionized water till the solution attains neutral pH. The solid

residue was repeatedly washed with ethanol and deionized water, and subsequently dried at 60 °C in vacuum to get a dark grey solid powder of GNRs. The synthesized GNRs powder was characterized by XRD, FTIR, HR-TEM and Raman spectral methods.

2.3 Synthesis of MLO using LO

For the synthesis of MLO, 20 ml of commercially available LO was taken into a 100 ml round bottom flask and 4 g of maleic anhydride was mixed to it. The mixture was subjected to malenization reaction by heating it at 210 ºC on an oil bath for 6 h under constant stirring to get a brown paste of MLO. The product was cooled to room temperature and the unreacted excess maleic anhydride was removed by solvent extraction process using water as a solvent. The thick brown semi-transparent paste of MLO was finally washed in distilled water and air dried for 24 h at 25 °C before being used as a coating material.

2.4 Preparation of MLO and MLO–GNR composite coatings on mild steel

Mild steel panels were first cut to small dimensions (4.0 cm × 2.0 cm) and abraded using different grades of sandpapers to get mirror shiny surface. They were degreased by subsequent washing with water and acetone, and then air dried at room temperature. MLO coating and MLO–GNR composite coatings were applied onto MS specimens by spin coating method.

For developing the MLO coatings, optimized stochiometric quantities (2:1) of MLO paste and hardener ((3-aminopropyl) triethoxysilane) were mixed uniformly and coated uniformly onto the as-prepared MS specimens using spin coating technique. The coated samples were first dried at room temperature for 24 h and then cured at 80 ºC for another 24 h. The cured samples were preserved in vacuum desiccators until further usage.

For the preparation of MLO–GNR nanocomposite, 1.0 gm MLO paste was weighed into a 100 ml beaker and dissolved in 20 ml ethanol. 0.5 wt% of GNRs powder was added to above MLO solution and the mixture was sonicated for 30 min to ensure the effective transfer of GNRs particles onto MLO. Further, the ethanol was removed by evaporation at room temperature to get brown solid paste of MLO–GNR composite. MLO–GNR composite coating was also applied on MS specimens using the same procedure as described for MLO coating.

2.5 Electrochemical investigations on anti-corrosive behaviour of coatings

The anti-corrosive behaviour of bare and coated MS samples in saline medium was studied using CH1608E electrochemical workstation. The three-electrode cell assembly comprising of Ag/AgCl (reference), platinum (counter electrode) and bare/coated mild steel specimens (working electrode) immersed in 3.5% NaCl electrolyte was employed as an electrode–electrolyte system. All open circuit potential (OCP), potentiodynamic polarization and electrochemical impedance spectroscopy (EIS) experiments were conducted on 1.0×1.0 cm^2 area of bare and MS-coated samples immersed in 3.5% NaCl medium. Potentiodynamic polarization measurements were conducted between the potentials -0.3 V and $+0.3$ V from open circuit potential at a scan rate of 2 mV min^{-1}. EIS measurements were performed at open circuit potentials in the frequency range between 100 kHz and 10 mHz with an sine-wave amplitude of 5 mV. The stability of MLO and MLO–GNR composite coatings were investigated by repeating Tafel polarization and EIS measurements for immersion time intervals of 2, 24 and 72 h.

3 Results and discussion

3.1 Physical characterization of GNRs

The dark powdery GNRs were synthesized by chemical unzipping of MWCNTs and structural characterization was performed by using electron microscopic and spectroscopic methods. Morphological features of MWCNT and the product GNRs were captured via HR-TEM analysis. The captured HR-TEM images of MWCNTs and GNRs are displayed in Fig. 1A and B, respectively. The inset pictures reveal magnified version of images. The captured image of MWCNTs displays smooth, tubular and undamaged surfaces, while that of product GNRs reveal two-dimensional damaged/wrinkled ribbon-like structures, thereby suggesting successful unzipping of MWCNTs into GNRs. The Raman spectral analysis of GNRs showed two intense bands (G and D) with much higher intensity compared to those revealed by MWCNTs (Fig. 1C). The higher band intensity ratio of GNRs ($I_D/I_G = 1.2$) compared to MWCNTs ($I_D/I_G = 0.8$) suggest certain degree of damages and deformations at the edges of GNRs structure as a result of unzipping of nanotubes. GNRs exhibit two major signals at $2\theta = 27°$ and $2\theta = 43°$ in their XRD spectrum (Fig. 1D) and the results are in agreement with literature [18, 20]. Contrary to this, XRD profile of MWCNTs show only one signal at $2\theta = 27°$ which explicitly indicate the successful
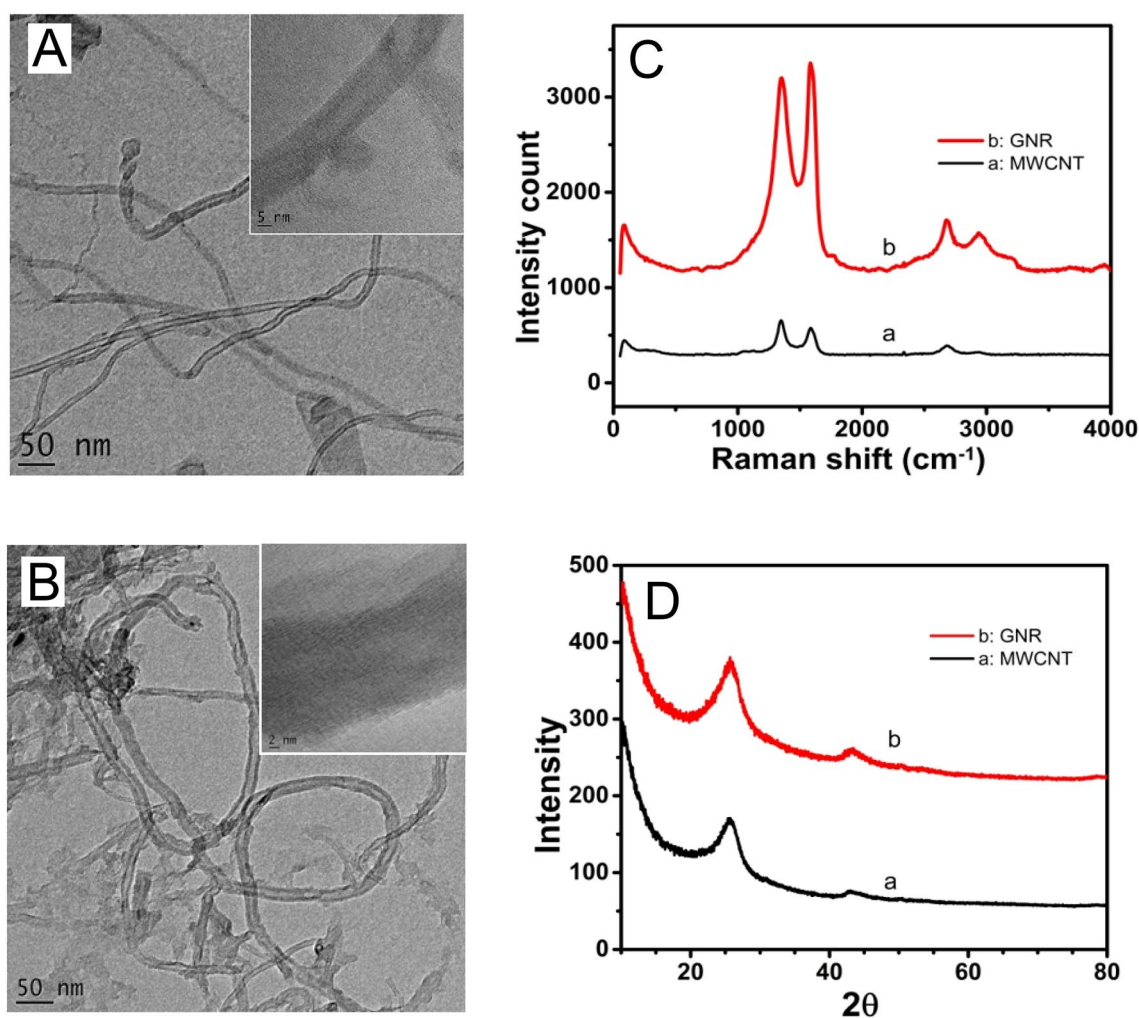
Fig. 1 HR-TEM image of MWCNT (**A**) and GNRs (**B**). Insets show magnified image; Raman (**C**) and XRD (**D**) profiles of MWCNT and GNRs

conversion of MWCNT into GNRs. The microscopic and spectroscopic data provide strong ample evidence on the successful unzipping of MWCNTs into GNRs.

3.2 Characterization of MLO

The successful synthesis of MLO from LO was confirmed through ^{1}H-NMR and FTIR characterization technique and the recorded ^{1}H-NMR spectra of LO and MLO are shown in Figs. S1 and S2, respectively. In the NMR spectra of LO, methylene hydrogens from the triglyceride moiety resonate to produce a multiplet signal around δ 4.14–4.34 ppm. The signal between 5.27 and 5.42 ppm appear correspond to the presence of vinyl hydrogens and methine hydrogen from the glyceride group. The NMR signals in the ^{1}H-NMR spectrum of MLO provide evidence for the formation of final product. The spectrum shows the newly generated proton peaks at δ 3.46–2.52 ppm indicating the attachment of diethylene tri-amine by ring opening of maleic anhydrides moiety in

the oil. The NMR results are in accordance with the earlier reported work on the synthesis of MLO from LO [27]. FTIR spectral analysis of reactants and products was performed to confirm the malenization of LO to MLO. FTIR spectrum (Fig. 2A) of LO reveals an IR signal at 3015 cm^{-1} ascribed to the =C–H stretching vibrations. The IR signals at 2920 and 2848 cm^{-1}, respectively, indicate asymmetric and symmetric stretching vibrations of methylene groups, while their signals corresponding to asymmetric and symmetric bending vibrations appeared in the positions 1467 and 1378 cm^{-1} respectively. The bond stretching vibrations of –C=C– produced a weak band at 1646 cm^{-1}. The bond stretching vibrations of C=O and C–O bonds of fatty acids have appeared as bands at 1743 and 1146 cm^{-1} positions. In the spectrum of LO, a prominent band at 1745 cm^{-1} is observed for the C=O group of triglycerides. Contrary to the LO spectral data, the FTIR spectral data of MLO appear to be slightly distinct (Fig. 2A). FTIR spectrum of MLO shows an additional band corresponding to –C=O stretching frequency. The new band
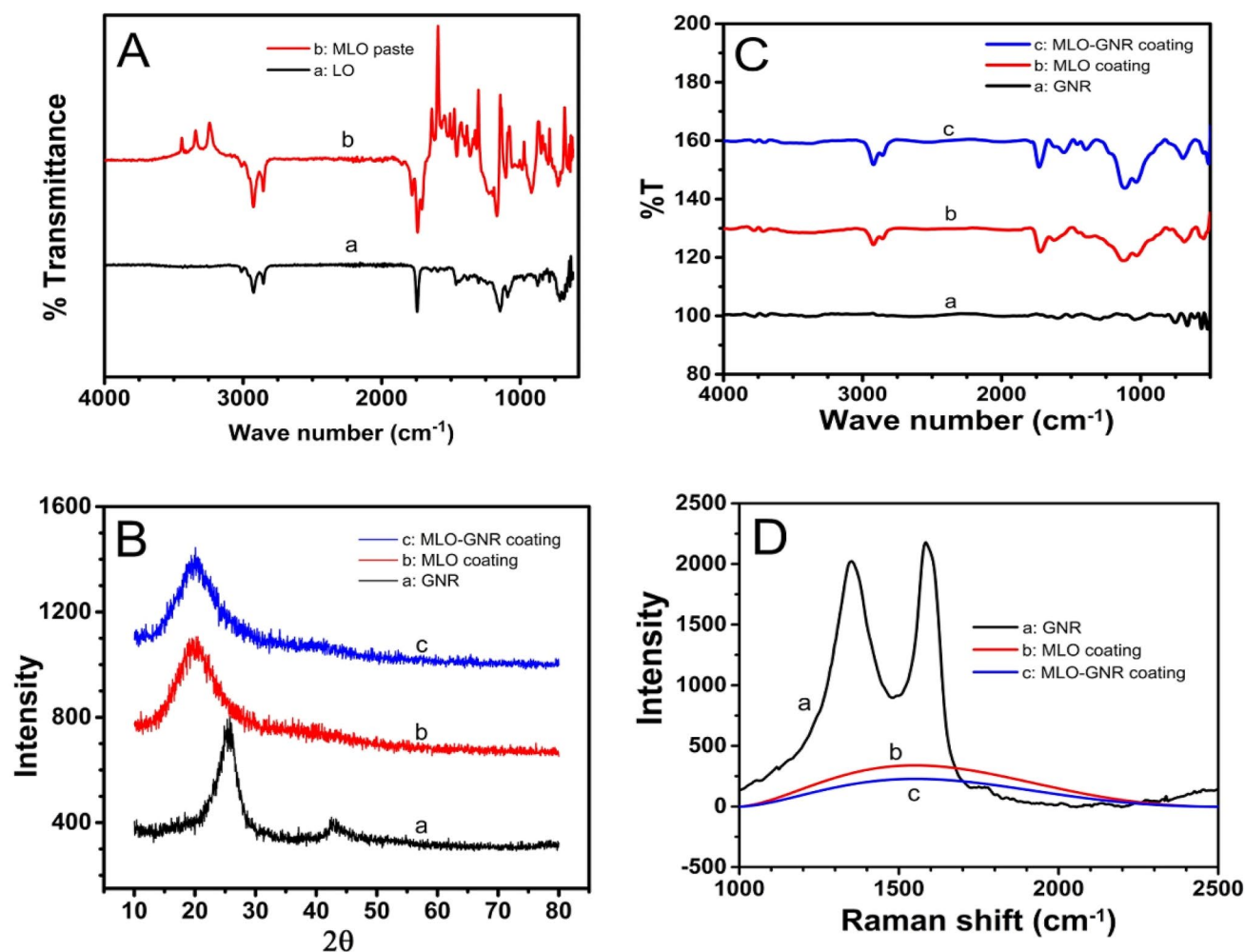
Fig. 2 **A** FTIR spectrum of LO and MLO paste, **B** XRD spectrum of GNR, MLO and MLO-GNR coating, **C** FTIR spectrum of GNR, MLO and MLO-GNR coating, **D** Raman spectrum of GNR, MLO and MLO-GNR coating

appears at 1780 cm^{-1} along with the C=O stretching band of triglycerides which can be solely attributed to the C=O stretching frequency of maleic anhydride moiety. This additional band in IR spectrum of MLO is a clear indication of successful attachment of maleic anhydride into the linseed oil backbone during malenization reaction. The mechanism of malenization of linseed oil [27] is shown in Scheme 1.

### 3.3 Physical and surface characterization of MLO and MLO–GNR coatings

3.3.1 X-ray diffraction studies

XRD studies on MLO coatings showed a dominant diffraction peak at $2\theta = 20°$ corresponding to the crystalline phase of MLO polymer network. Similarly, XRD profile of GNRs showed two diffraction peaks at 2θ values 27° and 43° suggesting its better crystalline character compared to MLO

coating. The incorporation of GNR into MLO matrix in small proportion (0.5%) produced a XRD profile similar to MLO coating revealing no significant changes in crystalline characteristics of MLO coating upon GNR incorporation (Fig. 2B).

3.3.2 FTIR and Raman characterization of coatings

FTIR analysis pure GNR, MLO coating and MLO–GNR coating were carried out and the FTIR spectral data are shown in Fig. 2C. The FTIR data of pure GNRs indicate feeble signals around the frequencies 1010, 1520 and 3700 cm^{-1} corresponding to C–O, C=C and –OH stretching vibrations of GNRs backbone and the edge groups on GNRs surface. FTIR spectrum of MLO shows prominent peaks at 1120 and 2920 cm^{-1} assignable to C–O stretching vibration and the asymmetric stretching vibrations of methylene group in MLO respectively. MLO spectrum shows
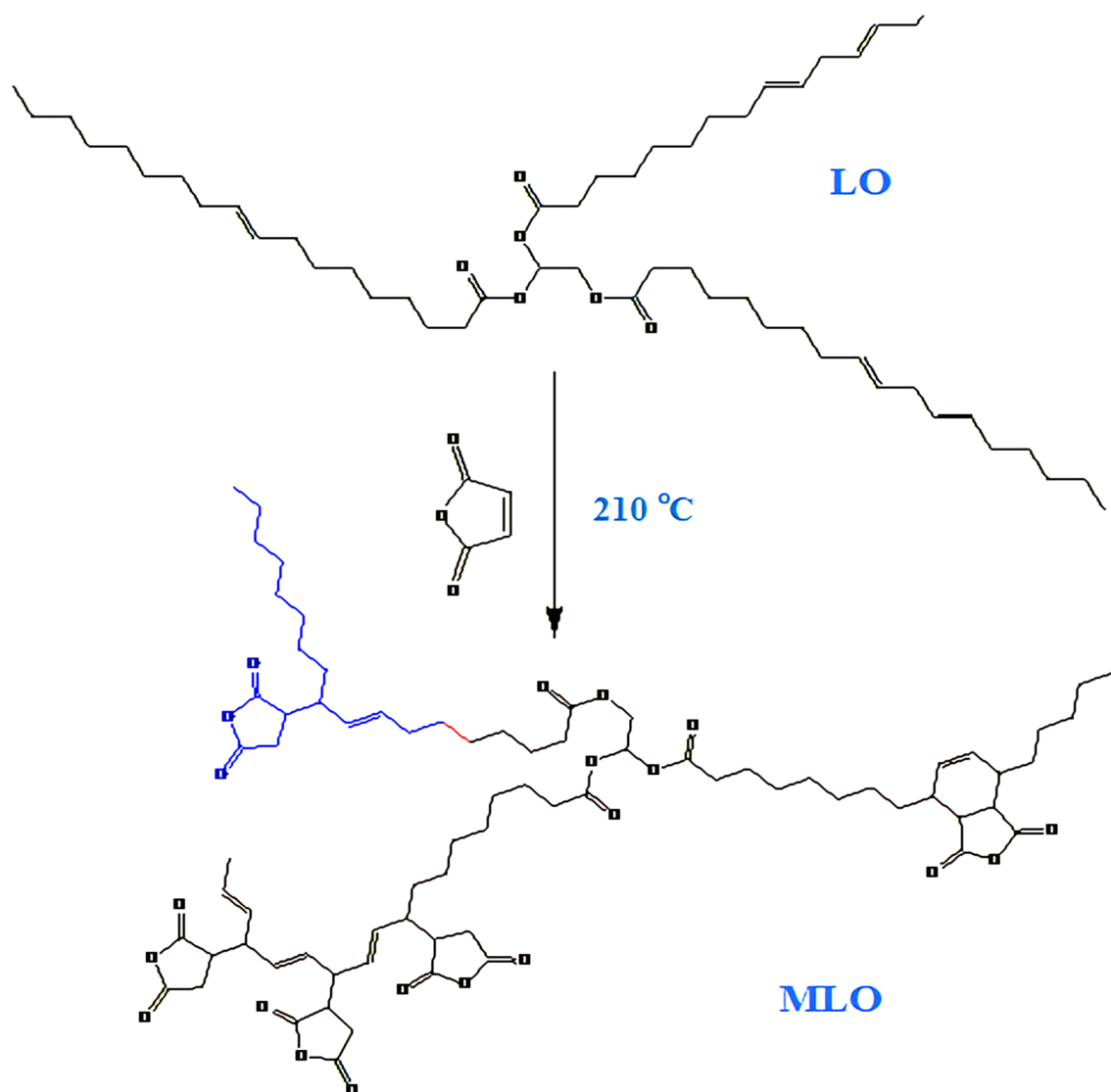
Scheme 1 Mechanism of malenization of LO

an additional band corresponding to –C=O stretching frequency at 1780 cm^{-1} along with the C=O stretching band of triglycerides which may be solely attributed to the C=O stretching frequency of maleic anhydride moiety.

On the other hand, the spectrum of MLO–GNR composite has lot of similarity to the spectrum of MLO. The signals of MLO–GNR coating almost have appeared at the same frequency as MLO coating. However, the signal intensity enhanced significantly possibly due to the interaction arising due to interaction between the MLO polymer backbone and the incorporated GNR sheets.

Raman spectrum of pure GNRs showed two intense G and D bands with band intensity ratio $I_D/I_G = 1.2$ (Fig. 2D). However, the Raman spectrum of MLO and MLO–GNRs did not produce the G and D bands (Fig. 2D). The absence of G and D bands in MLO–GNR composite coating was not

surprising considering the low concentration of GNRs used in the preparation of MLO–GNR composite.

3.3.3 AFM analysis

The roughness of surface is a crucial parameter that decides the coating characteristics such as wear resistance, surface adhesion, wettability and pitting susceptibility which in turn determines anti-corrosive behaviour of applied coatings. The surface roughness and surface topography of MLO and MLO–GNR composite coatings were investigated by AFM technique. The 3D-AFM micrographs of MLO and MLO–GNR coating are shown in figures Fig. 3A and D. The analysis of 3D-micrographic images of MLO coatings reveals rough and non-uniform surface with small hills and valley regions featured on the coating surface. On the other

Fig. 3 AFM image of MLO (**A**) and MLO-GNR (**B**) coatings. **C** TGA (*a*) and DTA (*b*) curves of thermal analysis data of MLO-GNR coating
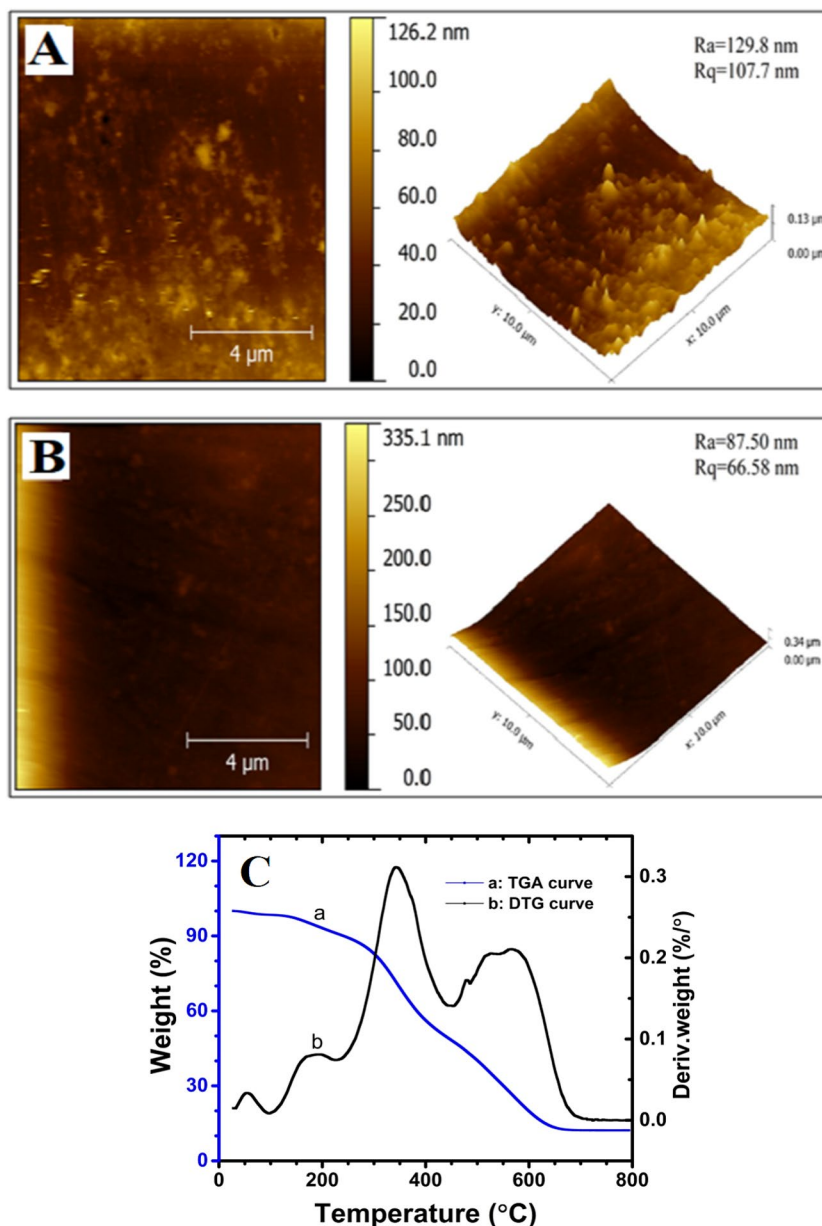
hand, MLO–GNR coating shows relatively smoother and uniform surface compared to MLO coating which lacks prominent hills and valley regions on its surface. The average roughness (R_a) and root mean square roughness (R_q) calculated from AFM data provides further evidence to support above topographic observations. The average roughness of MLO-coated specimen ($R_a = 129.8$ nm) was higher compared to MLO–GNR coating ($R_a = 87.5$ nm). The root mean square roughness of MLO coating also showed higher values ($R_q = 107.7$ nm) than that of MLO–GNR coating ($R_q = 66.58$ nm) suggesting better smoothness and uniformity for the MLO–GNR composite coating. These results clearly suggest that the roughness of coating surface reduced significantly upon the incorporation of GNR into

MLO polymer matrix. The GNR incorporation expectedly blocks the defected sites, improves adhesion and enhances the barrier properties of MLO polymer network to retard the corrosion rate. The literature also suggests that the coatings with higher surface roughness tend to promote corrosion reaction easily compared to smoother surfaces [28, 29]. Therefore, the AFM roughness data conclusively propose that the MLO-coated samples have greater corrosion tendency compared to MLO–GNR-coated samples.

3.3.4 Thermal stability study

Thermal stability of MLO–GNR composite coating was studied by performing TGA and DTA analysis in the

temperature range of 0–800 °C. The TGA and DTA data of MLO–GNR coating is presented as thermogram in Fig. 3C. The thermogram indicates a very high thermal stability for the coating in the temperature range of 0–250 °C. The thermal treatment in the temperature range 250–600 °C showed a drastic weight loss in the sample accounting for a net loss of 82%. Thermogravimetric data showed 18% ash content, 80% organic content and 2% moisture content for the sample. The observed weight reduction is purely attributed to the loss of moisture content and organic content. The differential thermogram revealed the presence of two major organic compounds in the sample which are thermally less stable at very high temperature. These compounds are arguably relatable to MLO polymer and the hardener employed in the development of MLO–GNR coating. These data are very well supported by the high ash content recorded in thermogravimetric analysis which is also evident from the highly organic nature of MLO–GNR coating. TGA and DTG

studies provide conclusive evidence on the high thermal stability of MLO–GNR coating in ultra-normal temperature up to 250 °C.

3.3.5 SEM studies of coating

The morphology and surface features of MLO and MLO–GNR coated MS samples were studied by SEM technique. The SEM micrograph of MLO and MLO–GNR composite-coated samples are shown in Fig. 4A and B, respectively. The micrographic image of MLO-coated specimen shows a smoother surface with very few defects on the surface. MLO–GNR composite coating show dense and compactly packed surface with lesser defects than MLO coating signalling that the MLO–GNR coating promises more protection to mild steel against corrosive agents. The digital images of MLO and MLO–GNR composite coatings before
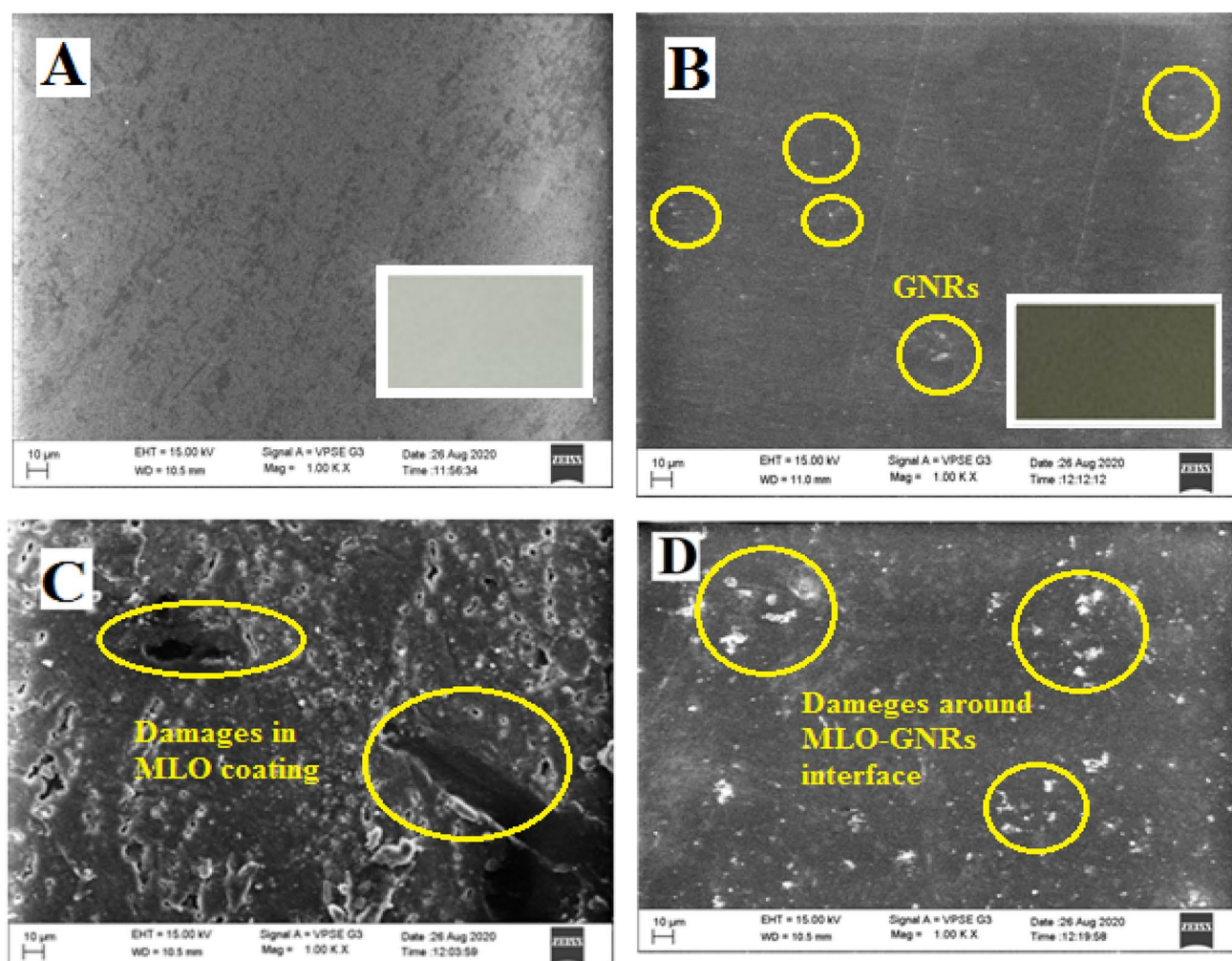

Fig. 4 SEM images with digital images (insets) of MLO coating (**A**) and MLO-GNR coating (**B**) before immersion in saline medium; SEM images of MLO coating (**C**) and MLO-GNR coating (**D**) after 72 h of immersion in saline medium

immersion in saline medium are shown as insets in Fig. 4A and B, respectively.

3.4 Evaluation of anti-corrosion behaviour of coatings

As the corrosion in saline medium occurs via electrochemical charge transfer processes, the anti-corrosion behaviour of bare and coated samples in 3.5% NaCl solution at different immersion times was examined by performing open circuit potential studies, potentiodynamic polarization and electrochemical impedance measurements.

3.4.1 Open circuit potential measurements

The OCP is the potential developed at the interface of coating/metal and the corrosion medium under zero current condition, and it provides insight into diffusibility of corrosive electrolyte into the coating/metal interface. The OCP values were recorded for bare and coated steel samples in 3.5% NaCl medium after prior immersion of samples for a period of 1 h and the results are presented as a plot of OCP vs run time in Fig. 5A. The results showed steady OCP responses for all samples and the response was more towards positive potential values for coated samples while it was more negative for the uncoated sample. The recorded OCP values of MS, MLO and MLO–GNR samples were -0.41 V, $+0.07$ V and $+0.13$ V, respectively. MLO-coated sample exhibited significantly higher OCP value than bare MS specimen suggesting the exhibition of high corrosion resistance by MLO coating. The OCP value of MLO–GNR composite-coated sample has shown more substantial shift to positive potential value compared to the other samples suggesting that the MLO–GNR composite coating more effectively resist the corrosion and prevent the diffusion of corrosive electrolyte. The higher OCP value of MLO–GNR composite is solely ascribed to the incorporation of GNR nanofiller into MLO polymer network. The validation of the observed anti-corrosive behaviour of coated samples was further confirmed by Tafel polarization experiments.

3.4.2 Potentiodynamic polarization studies

Potentiodynamic polarization experiments were conducted to determine the corrosion current density (I_{corr}), corrosion potential (E_{corr}) and the corrosion rates of bare and coated MS samples. The obtained experimental results are shown in the form of Tafel polarization curves in Fig. 5B. The potentiodynamic polarization curves of MLO and MLO–GNR composite-coated samples show a significant drift in the potentials to more positive side compared to uncoated MS specimen. The corrosion current densities of coated samples shifted to lower values suggesting a

decrease in corrosion activity at the coating–electrolyte interface. Further, the shift in E_{corr} and I_{corr} is more pronounced in MLO–GNR composite-coated sample compared to MLO-coated sample, thereby indicating highest corrosion prevention ability of the composite coating. Further, the polarization data reveal highest polarization resistance (R_p) and lowest corrosion rate (CR) for MLO–GNR composite coating. The polarization resistance enhanced above 200 folds and the corrosion rate reduced by over 2000 folds for MLO–GNR coating which clearly demonstrate the higher corrosion resistance exhibited by MLO–GNR composite coating in saline medium. The manifested robustness in corrosion resistance of MLO–GNR composite is presumed to be a combined effect of MLO polymer network and the GNR nanosheets in effectively shielding the transportation of electrons and chloride ions between the coated surface and electrolyte. The corrosion protection efficiency (PE) of different coatings were calculated from the current densities of blank ($I_{corr(blank)}$) and coated samples ($I_{corr(coat)}$) using the equation [17, 29]

$$PE(\%) = \left(\frac{I_{corr(blank)} - I_{corr(coat)}}{I_{corr(blank)}} \right) \times 100$$

The calculated protection efficiency was highest (99.9%) for the MLO–GNR composite coating, while a similar efficiency was also found for the MLO coating (99.95%). The blank MS specimen showed highest corrosion activity and experienced lowest protection compared to coated samples as evident from the polarization data. The experimental polarization data and calculated parameters such as corrosion potential, corrosion current density, anodic slope (b_a), cathodic slope (b_c), polarization resistance, corrosion rate and protection efficiency for different samples is summarized in Table 1.

The corrosion rate (CR) was estimated from the corrosion current values using the standard equation [17, 29].

$$CR = 87600 \left(\frac{E_w I_{corr}}{n \rho F} \right)$$

where I_{corr} is the corrosion current density (A cm^{-2}) obtained from Tafel curves, ρ is the density of steel (7.85 g cm^{-3}), E_w is the formula weight of mild steel (55.85 g mol^{-1}), F is the Faraday constant and n is the chemical valence of ferric ion.

The polarization resistance was calculated from the equation

$$R_p = \left(\frac{1}{2.303} \right) \frac{b_c b_c}{I_{corr}(b_a + b_c)}$$

where b_a and b_c are the Tafel constants measured from experimental data.
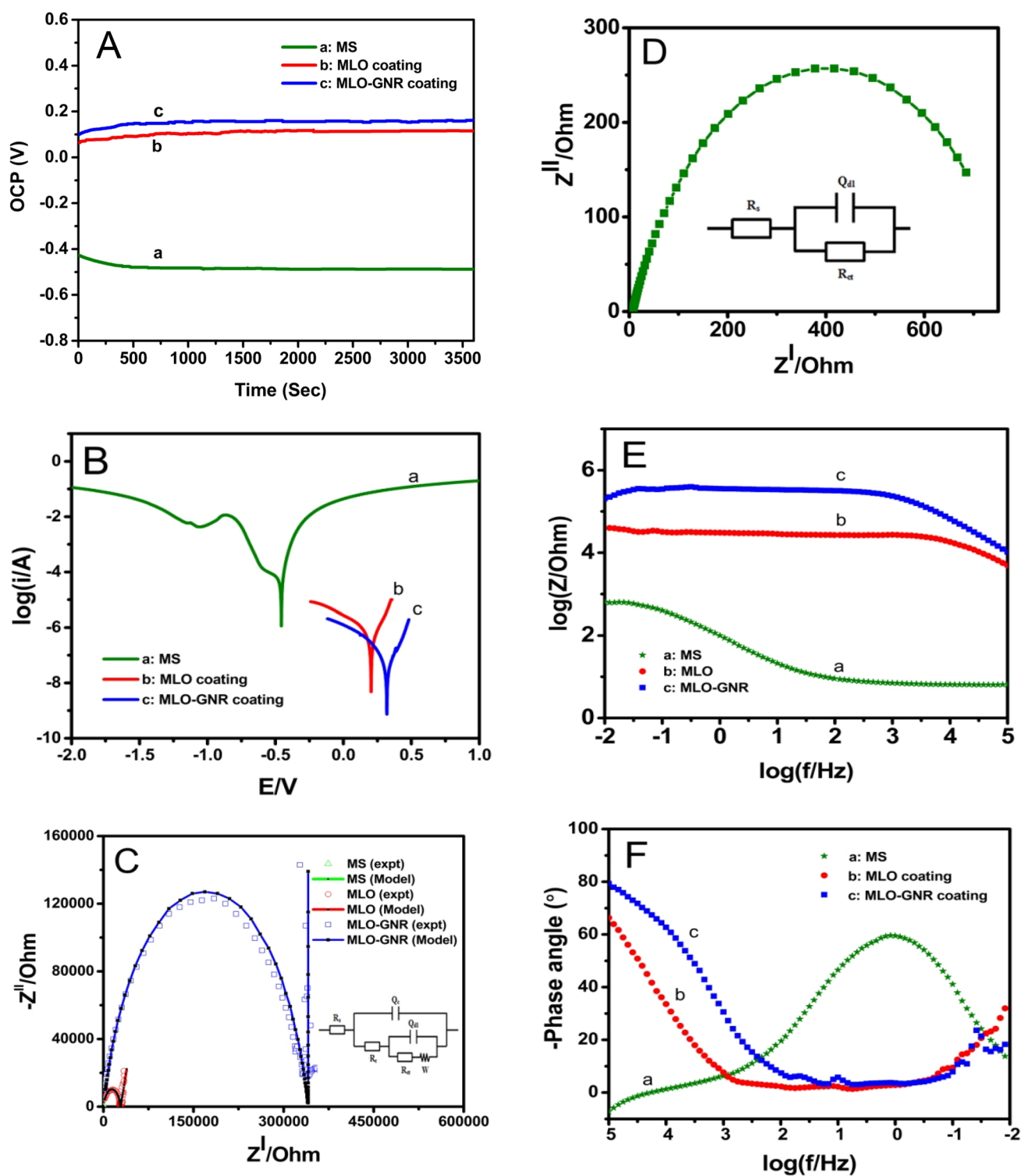
Fig. 5 Potentiodynamic polarization data of bare and coated MS samples: **A** Plot of OCP vs time, **B** Plots of Tafel polarization data, **C** Nyquist plots MS, MS-MLO, MS-MLO-GNR samples along with RQRQRW circuit diagram, **D** Magnified version of Nyquist plot of MS along with its RQR circuit diagram, **E** Bode impedance spectrum and **F** Bode phase angle diagram of bare and coated MS samples

Table 1 Potentiodynamic polarization data of bare and coated MS samples

Sample	E_{corr} (V)	I_{corr} (A/cm^2)	b_a (mV/dec^{-1})	b_c (mV/dec^{-1})	R_p (Ohm cm^2)	CR (mil/year)	PE (%)
MS	− 0.4566	1.163×10^{-4}	11.054	2.544	275	52.97	0
MS-MLO	+ 0.2036	4.525×10^{-7}	9.707	4.758	66,425	0.2061	99.6
MS-MLO-GNR	+ 0.3198	5.176×10^{-8}	9.013	6.366	546,195	0.02357	99.95

3.4.3 Electrochemical impedance studies

EIS technique is a powerful tool to probe the barrier properties, corrosion mechanism and the robustness of the coatings. EIS experiments were performed in the frequency range between 100 kHz and 10 mHz for different samples at their respective open circuit potentials and the obtained results are represented as Nyquist diagram (Fig. 5C and D). Bode impedance (Fig. 5E) and Bode phase angle (Fig. 5F) plots from EIS data assist in understanding the relative impedance characteristics of different specimens. The lowest frequency impedance modulus ($|Z|_{10\,mHz}$) value at 10 mHz in Bode impedance plot and the highest frequency phase angle ($|\theta|_{100\,kHz}$) value at 100 kHz in Bode phase angle plot are detrimental in deciding the anti-corrosive behaviour of coating in corrosive medium. Low-frequency impedance $|Z|_{10\,mHz}$ gives assessment of overall resistance (barrier effect) offered by the coating while acting as a barrier between the metal and corrosive medium. On the other hand, high-frequency phase angle $|\theta|_{100\,kHz}$ is indicative of pore resistance, i.e. resistance to the penetration of electrolyte into coating. Higher the values of $|Z|_{10\,mHz}$ and $|\theta|_{100\,kHz}$, better is the anti-corrosion performance of the coating. The $|Z|_{10\,mHz}$ values recorded for MS, MLO, MLO–GNR specimen are 6.38×10^2, 3.82×10^4 and 2.05×10^5 Ω, and the corresponding $|\theta|_{100\,kHz}$ values are 7.16, 66.3 and 79.3, respectively. These values clearly indicate better barrier properties for coated specimen compared to uncoated MS specimen. Comparatively, higher $|Z|_{10\,mHz}$ and $|\theta|_{100\,kHz}$ values observed for MLO–GNR composite coating indicate superior anti-corrosion ability of the coating which may be owed to well disperse GNR nanosheets in MLO matrix. The GNR nanosheets are presumed to enhance corrosion prevention capability of composite coating by effectively blocking the pores and enhancing the diffusion pathway of

electrolyte to metal surface. The lower $|Z|_{10\,mHz}$ and $|\theta|_{100\,kHz}$ values recorded for bare MS specimen are expected due to direct accessibility of metal surface to corrosive electrolyte.

Nyquist diagram of EIS data gives a qualitative assessment of extent of charge transfer phenomenon occurring at the interface of sample surface and its surrounding corrosive electrolyte. The semicircular region in a Nyquist curve give information on the charge transport phenomenon occurring at the specimen-electrolyte interface, while the linear portion of curve (if any) contains information on the diffusion phenomenon. The diameter of semicircle is proportional to charge transfer resistance (R_{ct}) and is inversely related to corrosion rate. In our experiments, Nyquist diagram of bare MS specimen (Fig. 5D) reveal smaller semicircle with lower diameter, whereas the coated samples recorded bigger semicircles of wider diameters (Fig. 5C). The wider diameters of coated samples suggest higher charge transfer resistance for the transportation of charged corrosive species from electrolyte to coated surface. Among the tested coatings, the semicircle recorded for MLO–GNR composite coating was much bigger in diameter compared to MLO coating implying relatively superior barrier protection and corrosion prevention properties for MLO–GNR composite.

A quantitative assessment of experimental EIS data was accomplished by fitting the data to suitable equivalent circuit models (Fig. 5C and D) using ZsimpWin software and the electrochemical parameters obtained from the simulated models are tabulated in Table 2. A closer look into experimental Nyquist and Bode phase angle diagrams of bare MS sample reveal the presence of one relaxation time in the medium-frequency regime, which indicate that the corrosion is controlled only by Faradic process (charge transfer process) at electrolyte–metal interface and the impedance data fits to equivalent electrical circuit with one-time constant. It was observed that the EIS data of uncoated MS specimen

Table 2 Impedance parameters of bare and coated MS samples fitted to RQR and RQRQRW equivalent circuit models

Sample	R_s (Ω cm^{-2})	Coating			Electrical double layer				Coating efficiency η(%)
		Q_c (S^{-n} cm^{-2})	n	R_c (Ω cm^{-2})	Q_{dl} (S^{-n} cm^{-2})	n	R_{ct} (Ω cm^{-2})	W (Ω cm^{-2})	
MS	6.711	–	–	–	2.578×10^{-3}	0.74	748.1	–	–
MS-MLO	6.28×10^{-4}	4.84×10^{-9}	0.79	2.85×10^4	2.66×10^{-4}	0.726	1.79×10^4	5.8×10^{-12}	95.82
MS-MLO-GNR	6.12×10^{-2}	1.39×10^{-10}	1.00	3.3×10^4	5.9×10^{-9}	0.668	3.06×10^5	1.8×10^{-5}	99.76

fitted perfectly to the model circuit $R_s(Q_{dl}R_{ct})$ with one-time constant, where R_s, Q_{dl} and R_{ct} represent solution resistance, double layer constant phase element and charge transfer resistance, respectively. The higher value of Q_{dl} obtained for MS specimen suggest that the metal surface acts as a perfect electrical double layer capacitance when immersed in ionic electrolyte. R_{ct} is a measure of resistance for charge transfer between the metal and the electrolyte and it is inversely proportional to the corrosion rate. The calculated R_{ct} value for MS sample based on $R_s(Q_{dl}R_{ct})$ model was 748.1 Ω cm^{-2} and other parameters are given in Table 2.

The experimental Nyquist and Bode phase diagrams of coated samples exhibited two-time relaxations, one close to low frequency and another one at high-frequency region. This means that the corrosion process is controlled by two parameters namely pore resistance of the coating and charge transfer control, and the impedance data fits to an equivalent electrical circuit with two-time constants. EIS data of coated samples after 2 h of immersion in 3.5% NaCl were found to fit perfectly to $R_s(Q_c(R_c(Q_{dl}(R_{ct}W))))$ electrical equivalent circuit model (Fig. 5C) with two-time constants, where R_s, Q_c, R_c, Q_{dl}, R_{ct} and W represent solution resistance, constant phase element of coating, coating or pore resistance, double layer constant phase element, charge transfer resistance and Warburg resistance, respectively. The calculated values of circuit parameters for MLO and MLO–GNR-coated samples based on the $R_s(Q_{dl}R_{ct})$ and $R_s(Q_c(R_c(Q_{dl}(R_{ct}W))))$ models are shown in Table 2.

3.4.4 Coating stability studies

The long-term stability is one of the essential features that decide durability and practical applicability of any coating. The long-time stability of MLO and MLO–GNR coatings were investigated by the potentiodynamic polarization and AC impedance methods by exposing the coated MS samples in 3.5% NaCl solution for 2, 24 and 72 h of prolonged immersion periods. The polarization and impedance responses recorded for MLO and MLO–GNR-coated samples at different immersion times are shown in Fig. 6A. Tafel curves from potentiodynamic polarization studies of both MLO and MLO–GNR-coated samples suggest that the long-time exposure of coated samples to saline conditions shifted the corrosion potentials to lower values and enhanced the corrosion current. The calculated polarization resistance showed a decreasing trend with exposure time which resulted in enhanced corrosion rates for the samples. The polarization data shown in Table 3 suggest reduction in protection efficiency of coating as a function of immersion time. Among the coated samples studied, MLO–GNR composite-coated sample exhibited relatively lower corrosion rates and higher protection efficiencies compared to MLO-coated sample after 2 h of immersion in 3.5% NaCl.

However, both these coatings exhibited reduced protection efficiencies against corrosion on further prolonged exposure to saline medium (Table 3). The results from polarization studies were further confirmed by conducting impedance studies. Bode and Nyquist impedance spectral plots for MLO and MLO–GNR composite coatings at different immersion times are shown in Fig. 6B and C, respectively.

These plots clearly suggest high overall impedance $|Z|_{10\,mHz}$ and lower phase angle $|\theta|_{100\,kHz}$ for both MLO and MLO–GNR-coated samples after 2 h of immersion. However, the prolonged exposure of these coatings to 24 and 72 h decreased $|Z|_{10\,mHz}$ and $|\theta|_{100\,kHz}$ values significantly which indicate reduction in protection efficiency of coatings, owing to prolonged exposure to corrosive agents in saline medium. MLO coating showed more pronounced reduction in $|Z|_{10\,mHz}$ and $|\theta|_{100\,kHz}$ values compared to MLO–GNR coating indicating higher stability for the MLO–GNR composite coating. A comparison of polarization and impedance parameters shown by different coatings at different exposure times is summarized in Table 3. The higher coating resistance shown by MLO–GNR is a result of incorporation of GNR to MLO matrix. The green polymer MLO applied on MS surface acted as an anti-corrosion barrier by preventing diffusion of corrosive species to MS surface. The incorporation of GNRs to MLO matrix has further enhanced the barrier properties by reducing the pore structure in the coating. The reduced porosity in polymer matrix prevents the easier entry of corrosive ions to metal surface. This causes enhancement in protection ability of MLO–GNR coating. However, prolonged exposure to corrosive medium damages the coating as this sets in swelling and delamination of coating. This gradually opened up the pores in coating and permits the easier diffusion of corrosive ions through pores of coating and attack metal surface. This led to failure of coating to protect the metal against attack of atmospheric agents.

The SEM micrographs of different coated samples before and after 72 h of exposure to 3.5% NaCl medium are shown in Fig. 4A–D. SEM images clearly show damages and morphological changes on coating surface upon subjection to 72 h of prolonged exposure to saline medium. Micrographic images show continuous, non-porous and crack-free smooth surfaces for the samples before exposure to saline medium. However, the SEM images of samples subjected to 72 h of prolonged exposure reveal cracks, severe damages and blistering of coating surface (Fig. 4C and D). The extent of damages is relatively higher for the MLO-coated sample compared to MLO–GNR-coated sample. This suggests that the presence of GNR enhances close packing in the MLO network and serve as a blockade for the entry of corrosive agents to the metal surface. However, both the MLO and MLO–GNR coatings, despite being damaged, showed high corrosion protection efficiency (above 90%) even after 72 h
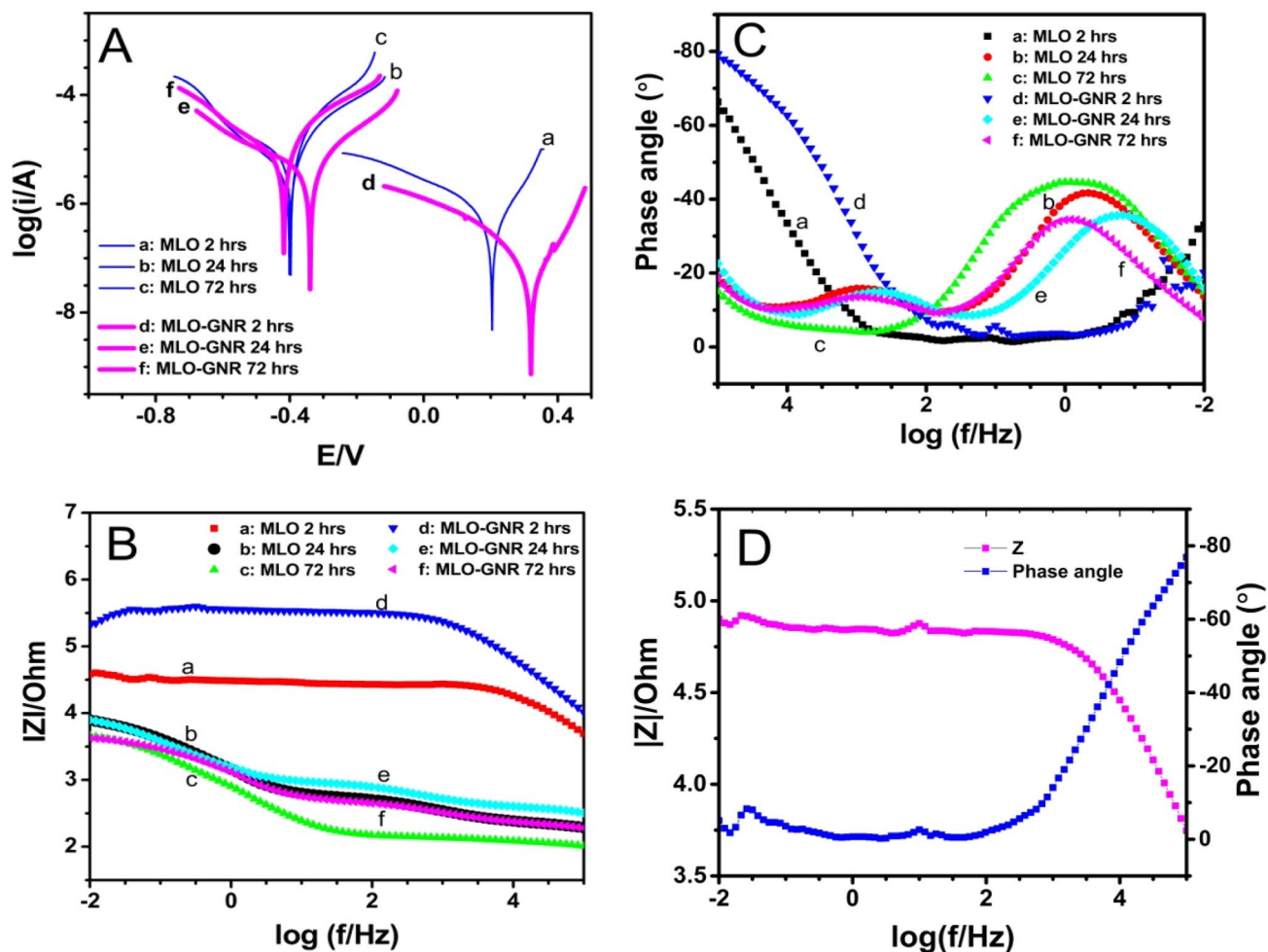
Fig. 6 Coating stability studies: Potentiodynamic polarization data (**A**), Bode impedance spectrum (**B**) and Bode phase angle diagram (**C**) of bare and coated MS samples after 2 h, 24 h and 72 h of immer-

sion in 3.5% NaCl medium; (**D**) Bode plot obtained for MLO-GNR coating after 6 months of open-air exposure

Table 3 Polarization and impedance data of coating stability studies in saline medium

Sample	Immersion time (hours)	E_{corr} (V)	I_{corr} (A cm^{-2})	R_p (Ω cm^{-2})	PE (%)	Corrosion rate (Mil/year)	$|Z|_{0.01\ Hz}$	θ
MLO coating	2 h	+0.2036	4.525×10^{-7}	66,425	99.60	0.2061	3.82×10^4	−66.3
	24 h	−0.4004	6.283×10^{-6}	6044	94.59	2.861	7.87×10^3	−19.3
	72 h	−0.3967	1.118×10^{-5}	3645	90.38	5.091	4.56×10^3	−15.0
MLO–GNR coating	2 h	+0.3198	5.176×10^{-8}	546,195	99.95	0.0236	2.05×10^5	−79.3
	24 h	−0.3389	5.87×10^{-6}	8309	94.95	2.675	7.93×10^3	−22.6
	72 h	−0.4178	1.034×10^{-5}	4042	91.11	4.710	4.25×10^3	−18.6

of prolonged exposure. These results gave conclusive evidence that MLO–GNR coating show superior anti-corrosive behaviour in saline medium.

To further assess the stability of MLO–GNR coatings in open-air environments, the MLO–GNR composite-coated MS sample was exposed to open atmosphere for a

period of 6 months and its Bode impedance and Bode phase angle responses were recorded at the end of 6 months. The recorded Bode impedance (7.9×10^{-4} Hz) and Bode phase angle ($-76.9°$) responses for MLO–GNR coating (Fig. 6D) showed no significant deviation from those of MLO–GNR coating recorded is saline medium. This suggests that the

MLO–GNR coating possess excellent long-term open-air stability and can be employed for the protection of iron and steel structures in open environments. Based on these results, it is concluded that the MLO–GNR nanocomposite exhibit excellent barrier protection properties and has the potential to be employed as an efficient anti-corrosive coating material for the protection of iron metal structures in domestic and industrial applications.

4 Conclusions

In the present work, a thick brown semi-transparent paste of MLO was developed by subjecting the bio-based LO to malenization reaction. Subsequently, the GNRs synthesized by the oxidative unzipping of MWCNTs were incorporated into the paste of MLO by a simple sonication method to get dark brown paste of MLO–GNR nanocomposite. Further, the as-prepared bio-based MLO and MLO–GNR composite materials were explored as a barrier layer on mild steel to reduce its corrosion. The anti-corrosion behaviour of MLO and MLO–GNR composite coatings on mild steel in 3.5% NaCl solution was evaluated by performing potentiodynamic polarization and impedance measurements. Both MLO and MLO–GNR-coated mild steel showed higher corrosion potential, higher polarization resistance, lower corrosion current and lower corrosion rates compared to uncoated mild steel substrate sample. MLO and MLO–GNRs coatings exhibited protection efficiencies of 99.6% and 99.95%, respectively, suggesting that they acted as an efficient anti-corrosion barrier for the substrate. Further, MLO–GNR nanocomposite-coated sample exhibited far superior protection capability and barrier properties compared to MLO-coated sample which is solely attributed to incorporated GNRs nanofiller. The investigations with prolonged exposure of coated samples to saline medium showed reasonable stability in 3.5 wt% NaCl solution up to 3 days though depletion and morphological changes have set-in in the coating after first day of immersion. Based on the observations from the study, it is concluded that the bio-based MLO coatings can effectively decrease the corrosion of mild steel and the incorporation of GNRs to MLO in appropriate proportions can further enhance anti-corrosion behaviour of coating. It is further concluded that unexplored 2D nanomaterial GNR emerge as the effective and promising alternative nanofiller in corrosion prevention applications. Further, this study established that there is plenty of scope for utilizing GNR and its structural derivatives or its various nanocompositions in future research for development of improved anti-corrosion coatings.

Author contribution NKS: Investigation, Writing—original draft. KNSM: Review and editing, Validation, Supervision. MBH: Methodology. AMM: Resources.

Declarations

Conflict of interest The authors declare that they have no conflicts of interest to disclose.

References

1. Sahu SC, Samantara AK, Seth M, Parwaiz S, Singh BP, Rath PC, Jena BK (2013) A facile electrochemical approach for development of highly corrosion protective coatings using graphene nanosheets. Electrochem Commun 32:22–26. https://doi.org/10.1016/j.elecom.2013.03.032

2. Gray JE, Luan B (2002) Protective coatings on magnesium and its alloys—a critical review. J Alloy Compd 336:88–113. https://doi.org/10.1016/S0925-8388(01)01899-0

3. Guo SF, Zhang HJ, Liu Z, Chen W, Xie SF (2012) Corrosion resistances of amorphous and crystalline Zr-based alloys in simulated seawater. Electrochem Commun 24:39–42. https://doi.org/10.1016/j.elecom.2012.08.006

4. Ramezanzadeh B, Niroumandrad S, Ahmadi A, Mahdavian M, Mohamadzadeh Moghadam MH (2016) Enhancement of barrier and corrosion protection performance of an epoxy coating through wet transfer of amino functionalized graphene oxide. Corros Sci 103:283–304. https://doi.org/10.1016/j.corsci.2015.11.033

5. Umoren SA, Solomon MM, Obot IB, Suleiman RK (2019) A critical review on the recent studies on plant biomaterials as corrosion inhibitors for industrial metals. J Ind Eng Chem 76:91–115. https://doi.org/10.1016/j.jiec.2019.03.057

6. Madhusudhana AM, Mohana KN, Hegde MB, Nayak SR, Rajitha K, Swamy NK (2020) Functionalized graphene oxide-epoxy phenolic novolac nanocomposite: an efficient anticorrosion coating on mild steel in saline medium. Adv Compos Hybrid Mater 3:141–155. https://doi.org/10.1007/s42114-020-00142-8

7. Rajitha K, Mohana KN, Hegde MB, Nayak SR, Swamy NK (2020) Fabrication of ZnO/rGO and ZnO/MWCNT nanohybrids to reinforce the anticorrosion performance of polyurethane coating. Flatchem 24:100208. https://doi.org/10.1016/j.flatc.2020.100208

8. Dinker A, Agarwal M, Agarwal GD (2017) Preparation, characterization, and performance study of beeswax/expanded graphite composite as thermal storage material. Exp Heat Transfer 30:139–150. https://doi.org/10.1080/08916152.2016.1185198

9. Atta AM, Al-Hodan HA, Hameed RSA, Ezzat AO (2017) Preparation of green cardanol-based epoxy and hardener as primer coatings for petroleum and gas steel in marine environment. Prog Org Coat 111:283–293. https://doi.org/10.1016/j.porgcoat.2017.06.002

10. Lligadas G, Ronda JC, Galià M, Cádiz V (2013) Renewable polymeric materials from vegetable oils: a perspective. Mater Today 16:337–343. https://doi.org/10.1016/j.mattod.2013.08.016

11. Alam M, Akram D, Sharmin E, Zafar F, Ahmad S (2014) Vegetable oil based eco-friendly coating materials: a review article. Arab J Chem 7:469–479. https://doi.org/10.1016/j.arabjc.2013.12.023

12. Ding C, Matharu AS (2014) Recent developments on biobased curing agents: a review of their preparation and use. ACS Sustain Chem Eng 2:2217–2236. https://doi.org/10.1021/sc500478f

13. Espinosa LMD, Meier MAR (2011) Plant oils: the perfect renewable resource for polymer science?! Eur Polym J 47:837–852. https://doi.org/10.1016/j.eurpolymj.2010.11.020

14. Hegde MB, Nayak SR, Mohana KN, Swamy NK (2020) *Garcinia gummigutta* vegetable oil-graphene oxide nanocomposite: an efficient and eco-friendly material for corrosion prevention of mild steel in saline medium. J Polym Environ 28:483–499. https://doi.org/10.1007/s10924-019-01611-y

15. Thanawala K, Mutneja N, Khanna AS, Singh RK (2014) Development of self-healing coatings based on linseed oil as autonomous repairing agent for corrosion resistance. Materials 7:7324–7338. https://doi.org/10.3390/ma7117324

16. Khandelwal V, Sahoo SK, Kumar A, Sethi SK, Manik G (2019) Bio-sourced electrically conductive epoxidized linseed oil based composites filled with polyaniline and carbon nanotubes. Compos B Eng 172:76–82. https://doi.org/10.1016/j.compositesb.2019.05.050

17. Madhusudhana AM, Mohana KN, Hegde MB, Nayak SR, Rajitha K, Swamy NK (2020) Development of Al_2O_3.ZnO/GO-phenolic formaldehyde amine derivative nanocomposite: a new hybrid anti-corrosion coating material for mild steel. Colloids Surf A Physicochem Eng Asp 601:125036. https://doi.org/10.1016/j.colsurfa.2020.125036

18. Sandeep S, Santhosh AS, Swamy NK, Suresh GS, Melo JS, Chamaraja NA (2018) A biosensor based on a graphene nanoribbon/silver nanoparticle/polyphenol oxidase composite matrix on a graphite electrode: application in the analysis of catechol in green tea samples. New J Chem 42:16620–16629. https://doi.org/10.1039/c8nj02325e

19. Asha PJ, Sabu C, Swamy NK, Anto A, Gangadharappa HV, Pramod K (2021) Graphene nanoribbon: an emerging and efficient flat molecular platform for advanced biosensing. Biosens Bioelectron 184:113245. https://doi.org/10.1016/j.bios.2021.113245

20. Swamy NK, Mohana KN, Hegde MB, Madhusudhana AM, Nayak SR, Rajitha K (2021) Fabrication of graphene nanoribbon-based enzyme-free electrochemical sensor for the sensitive and selective analysis of rutin in tablets. J Appl Electrochem 51:1047–1057. https://doi.org/10.1007/s10800-021-01557-x

21. Habibpour S, Um JG, Jun Y, Bhargava P, Park CB, Yu A (2021) Structural impact of graphene nanoribbon on mechanical properties and anti-corrosion performance of polyurethane nanocomposites. Chem Eng J 405:126858. https://doi.org/10.1016/j.cej.2020.126858

22. Arjmand M, Sadeghi S, Navas IO, Keteklahijani YZ, Dordanihaghighi S, Sundararaj U (2019) Carbon nanotube versus graphene nanoribbon: impact of nanofiller geometry on electromagnetic interference shielding of polyvinylidene fluoride nanocomposites. Polymers 11:1064. https://doi.org/10.3390/polym11061064

23. Tour J, Sikkema WA, Metzger A, Wang T (2017) Physical and electrical characterization of Texas PEG: an electrically conductive neuronal scaffold. Surg Neurol Int 8:84. https://doi.org/10.4103/sni.sni_361_16

24. Swamy NK, Mohana KN, Yashas SR (2022) GNR@CeO_2 heterojunction as a novel sonophotocatalyst: degradation of tetracycline hydrochloride, kinetic modeling and synergistic effects. Colloids Surf A Physicochem Eng Asp 639:128324. https://doi.org/10.1016/j.colsurfa.2022.128324

25. Sanjay BP, Sandeep S, Santhosh AS, Karthik CS, Varun DN, Swamy NK, Mallu P, Nithin KS, Rajabathar JR, Muthusamy K (2022) Unprecedented 2D GNR-CoB nanocomposite for detection and degradation of malachite green-A computational prediction of degradation pathway and toxicity. Chemosphere 287:132153. https://doi.org/10.1016/j.chemosphere.2021.132153

26. Kosynkin DV, Higginbotham AL, Sinitskii A, Lomeda JR, Dimiev A, Price BK, Tour JM (2009) Longitudinal unzipping of carbon nanotubes to form graphene nanoribbons. Nature 458:872–876. https://doi.org/10.1038/nature07872

27. Fombuena V, Petrucci R, Dominici F, Jordá-Vilaplana A, Montanes N, Torre L (2019) Maleinized linseed oil as epoxy resin hardener for composites with high bio content obtained from linen by products. Polymers 11:301. https://doi.org/10.3390/polym11020301

28. Figueira RB, Silva CJR, Pereira EV (2016) Hybrid sol–gel coatings for corrosion protection of galvanized steel in simulated concrete pore solution. J Coat Technol Res 13:355–373. https://doi.org/10.1007/s11998-015-9751-7

29. Rajitha K, Mohana KN, Mohanan A, Madhusudhana AM (2020) Evaluation of anticorrosion performance of modified gelatin-graphene oxide nanocomposite dispersed in epoxy coating on mild steel in saline media. Colloids Surf A Physicochem Eng Asp 587:124341. https://doi.org/10.1016/j.colsurfa.2019.124341